Ordered Binary Arrays of Au Nanoparticles Derived from Colloidal Lithography

Gang Zhang, Dayang Wang,* and Helmuth Möhwald

Max Planck Institute of Colloids and Interfaces, D-14424 Potsdam, Germany

Received September 28, 2006; Revised Manuscript Received November 30, 2006

ABSTRACT

By using angle-resolved colloidal lithography and O_2-plasma etched bilayers of hexagonally packed spheres as templates, we succeeded in fabrication of highly ordered binary arrays of gold nanoparticles with varied shapes, for instance, with a shuttlecock-like shape composed of a small crescent-shaped nanoparticle and a big fan-shaped one. The size and shape of both small and big nanoparticles obtained were manipulated by the plasma etching period and the incidence angle of Au vapor flow. The subsequent thermal annealing led to binary arrays of round Au nanoparticles with a rather narrow distribution in terms of size and shape. Our approach should pave a simple and versatile colloidal way to form binary nanoparticle arrays, holding immense promise for technical applications such as nanoelectronics and nanophotonics.

Fabrication of ordered arrays of inorganic nanoparticles is of significance for both fundamental science associated with low-dimensional physics and technical applications.[1] Up-to-date lithography is the major workhorse of generating nanoparticle arrays. Nonetheless, the lithographic techniques are fairly expensive, complicated, and time-consuming, especially for generation of large-area samples.[2] Although soft lithography allows facile generation of various patterns, it is hard to fabricate pattern features smaller than 100 nm and over a large area.[2c]

Monodisperse spheres of submicrons to microns in size can readily self-assemble into highly ordered and close-packed arrays, so-called colloidal crystals.[3] By using the ordered interstitial arrays within colloidal crystals as masks, one has succeeded in sculpturing hexagonal arrays of monodisperse nanoparticles with the shape of a pyramid, ring, or rod on planar substrates, paving a colloidal lithography way.[4−7] This enables rather facile and cheap fabrication of periodic nanostructures over large areas as compared to conventional lithography. The size and shape of metallic nanoparticles are dependent on the projection of the interstices in colloidal crystals and can in turn be easily manipulated by the size and packing symmetry of the template spheres. Furthermore, the incidence angle of the metal vapor flow also provides an exquisite measure to control the size and shape of the nanoparticles obtained.[4c] This is referred to as angled-resolved colloidal lithography. Because the voids between monodisperse spheres in colloidal crystals are uniform in size, however, the existing colloidal lithographic techniques allow only construction of periodic arrays of nanoparticles of one size; no binary array was obtained thus far. To circumvent this challenge, herein we employed O_2-plasma etched bilayers of hexagonally closely packed polystyrene (PS) spheres as masks during Au vapor deposition. The manipulation of the incidence angle of Au vapor flow led to binary periodic arrays of Au nanoparticles.

Plasma etching can efficaciously engineer the structures of colloidal crystals, including the shape of spheres and interstices and the spacing of neighboring spheres.[8] Prior to Au vapor deposition, in the current work, the bilayers of hexagonally close-packed 830 nm PS spheres were etched by O_2-plasma for different lengths of time. Subsequently, they were used as masks for Au vapor deposition at the incidence angle of 15°. After decomposition of the PS bilayer masks with toluene, the resulting Au nanostructures were visualized by scanning electron microscopy (SEM). When the bilayer masks were etched by O_2-plasma for less than 30 min, intriguingly, Au nanoparticles with a shuttlecock-like shape were obtained, which were arranged in a long-range hexagonal array with a periodicity of 830 nm over a large area (Figure S1a, Supporting Information). The nano-sized Au shuttlecocks were composed of two differently sized nanoparticles separated by a tiny gap, a small one with a crescent shape and a big one with a fan shape. The comparison of parts a, b, and c of Figure 1 reveals that the dimension of both the small and the big Au nanoparticle slightly increases with the etching time of the bilayer masks (Table 1). Nonetheless, the center-to-center distance between the small and big nanoparticle was little changed, close to 350 nm. When the etching period was longer than 30 min,

* To whom the correspondence should be addressed: E-mail: dayang.wang@mpikg-golm.mpg.de. Fax: (+49) 331 567 9202.
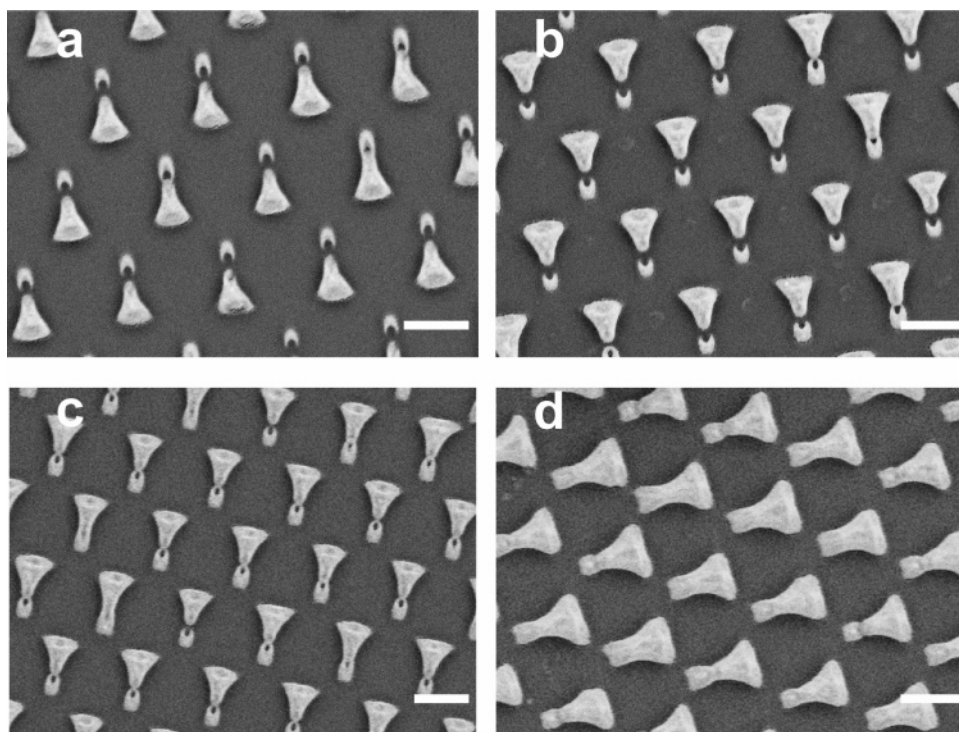
Figure 1. SEM pictures of hexagonally arranged Au nanoshuttlecocks obtained by using bilayers of hexagonal close-packed 830 nm PS spheres, etched by O_2 plasma for 10 (a), 20 (b), 25 (c), and 30 min (d), as masks for Au vapor deposition. The incidence angle of Au vapor flow was set as 15°. The scale bars are 500 nm.

Table 1. Summary of the Dimension of the Spheres in Etched 830 nm PS Sphere Bilayers and the Nanoparticles Derived from Them.

samples	etching time (min)	θ	R (nm)	R_1 (nm)	R_2 (nm)	a (nm) calcd value[g]		a (nm) exptl value	b (nm) calcd value[h]	b (nm) exptl value
1[a]	10	15°	415	330	387	40.8	105.1[i]	95	318.2	362
2[b]	20	15°	415	313	380	49.7	109.2[i]	106	325.4	370
3[c]	25	15°	415	295	375	59.7	114.1[i]	128	330.6	378
4[d]	30	15°	415	250	360	81.8	122.0[i]	214	346.1	452
5[e]	20	30°	415	313	380	167.0	194.1[i]	250	280.0	305
6[f]	20	45°	415	313	380	297.6	289.3[i]	271	181.3	136

[a] The SEM picture is shown in Figure 1a. [b] The SEM picture is shown in Figure 1b. [c] The SEM picture is shown in Figure 1c. [d] The SEM picture is shown in Figure 1d. [e] The SEM picture is shown in Figure 5a. [f] The SEM picture is shown in Figure 5c. [g] It is calculated by eq 1. [h] It is calculated by eq 2. [i] The diameter of the upper spheres was assumed as 70% of R_1

the small and big nanoparticles were eventually fused together into one spoon-shaped particle (Figure 1d). Figure S1a (Supporting Information) shows that a handful of small crescent-shaped Au nanoparticles were slightly merged with big fan-shaped particles, even fused into big spoon-shaped particles. This should be due to the packing defect of the colloidal crystal masks.

To correlate the interstitial structures in the etched bilayers of hexagonally close-packed PS spheres with the Au nanoshuttlecocks, the spheres, especially in the lower layers, were partially peeled off with Scotch tape (Figure 2). In Figure 2, the upper-layer spheres are highlighted by the blue circles and the incidence direction of the Au vapor flow by an orange arrow, registered based on the orientation of Au patterns formed on the lower-layer spheres.[9] In a hexagonally close-packed sphere bilayer, every other 3-fold interstice

(highlighted by yellow circles in Figure 2) in the lower layer is blocked by the upper-layer sphere (highlighted by the blue circle), leaving behind a 6-fold array of interstitial channels (highlighted by the red circles). Their use as masks for colloidal lithography led to hexagonal arrays of Au nanoparticles.[4] As shown in Figure 2, in contrast, after the bilayers were etched by O_2-plasma, all of the voids between the lower-layer spheres allow diffusion of Au vapor to form Au nanoparticles; the big particles were derived from the unblocked voids and the small ones from the blocked voids along the incidence of Au vapor. This can be due to the anisotropic character of plasma etching of colloidal crystals, namely, the upper-layer spheres and the voids between the spheres in close-packed sphere bilayers were etched more than the lower layer spheres. The plasma etching opens small gaps between the upper layer spheres and their blocked voids
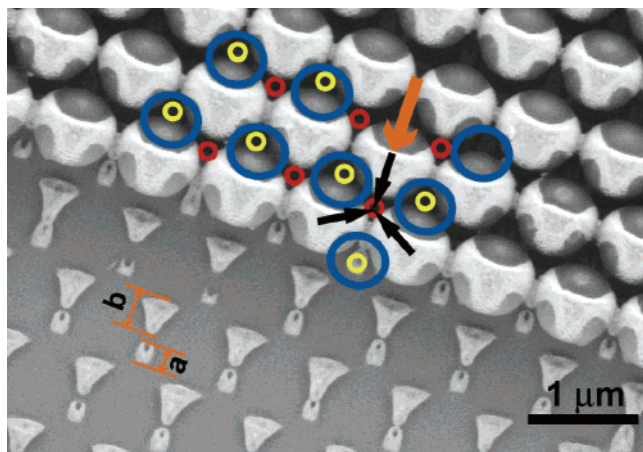
Figure 2. SEM image of coexistence of Au nanoshuttlecocks and the lower spheres with an Au patterned surface, obtained by partially peeling off the PS spheres. The areas, where upper-layer spheres were completely peeled off, are marked by blue circles. The voids in the lower layer, blocked by the upper-layer spheres, are highlighted by yellow circles, and the unblocked voids by red circles. The orange arrow indicates the incidence direction of Au vapor flow, and the black ones indicate the direction of the vector from the sphere center to the void center in the lower layer. The lengths of the small crescent-shaped and the big fan-shaped nanoparticles are underlined and marked as *a* and *b*.

in the lower layer. Through these gaps, the incidence angle of 15° may allow diffusion of Au vapor into the blocked voids in the lower layers, thereby resulting in small Au nanoparticles (Figures 1 and 2). By controling the O_2-plasma intensity and the etching period, close-packed PS sphere bilayers were so slightly etched that the spheres in the lower layer remained close-packed. The projection of the joints between them resulted in gaps interspaced between small and big nanoparticles (Figure 1a,b,c). When the bilayers were etched for longer than 30 min, in our work, the spheres in the lower layer turned non-close-packed and thus caused fusion of the small and big nanoparticles (Figure 1d). Because the gaps, opened via plasma etching, were envisioned as still underneath the upper-layer spheres, metal vapor was not able to diffuse into the blocked voids in the lower layers by normal incidence; only hexagonal arrays of nanoparticles were obtained similar to those derived from non-etched bilayers.[10] Note that the coincidence of the direction of the Au vapor incidence with that of the vector from the sphere center to the void center in the lower layer, underlined by a black arrow in Figure 2, is prerequisite to construct Au nanoshuttlecocks. To achieve this coincidence, in our work, the sphere-packing orientations of bilayers therefore were determined by SEM prior to Au vapor deposition.

Because of anisotropic plasma etching, the joint parts between the neighboring spheres with colloidal crystal masks were etched less severely than the sphere edge around the interstices. Accordingly, the joint bars were formed between the lower layer spheres to shield Au vapor (Figure S2, Supporting Information). Accordingly, shielding of these joint bars led to the gaps between the small and big Au nanoparticles during Au vapor deposition at the nonzero

incidence. The dimension of the joint bars was expected to decrease with the increase of plasma etching time, thus shortening the spacing between the small and big particles, as shown in Figure 1. On the other hand, one may expect that the joint bars between the lower-layer spheres shielded the penetration of the Au vapor into the opening between the upper-layer spheres and their blocked voids in the lower layer along the incidence of the Au vapor at a nonzero incidence angle. As a result, a round shape with a gap at the edge, namely a crescent-shape, should be formed for small Au nanoparticles.

The Au nanoshuttlecocks obtained above were annealed at high temperature with the intent to improve the uniformity of the constituent nanoparticles. As compared to that of the corresponding bulk materials, the melting point of nanoparticles is much lower and especially more sensitive to surface tension. Because the large curvature causes a high surface tension, the annealing of nonround nanoparticles may give rise to a retraction of their apexes, eventually generating a round shape.[7b] Accordingly, we found that, after annealing at 700 °C for 60 min in ambient, both small crescent-shaped and big fan-shaped nanoparticles of Au nanosized shuttlecocks retracted into polygon particles; the original shape was still visible by the residual traces (Figure S3, Supporting Information). The annealing at 900 °C for 60 min in ambient led to hexagonally arranged arrays of small and big Au nanoparticles with a nearly round shape (Figure 3a,b,c). Their periodicity remained little varied, about 830 nm. As compared to the original nanoparticles, the round nanoparticles, both small and big ones, were much smaller and exhibited a pronounced size dependence on the plasma etching time. Although the spacing distance between the small and big nanoparticles dramatically increased, the center-to-center distances were fairly comparable to those before annealing. Similarly, the annealing transformed spoon-shaped nanoparticles into round nanoparticles arranged in a hexagonal array (Figure 3d). The comparison between Figures 1 and 3 reveals that the patterning blurring was efficiently eliminated by the postannealing. Note that, during the postannealing, a slight merging caused fusion of small crescent-shaped nanoparticles with big fan-shaped particles to round large particles. Depending on the packing defect density of the colloidal crystal masks, about 10−30% of small particles disappeared after annealing (Figure S1b, Supporting Information).

To quantitative assess the influence of experimental variables, particularly the incidence angle of Au vapor flow (θ), on the shape and size of Au nanoparticles, we implemented a geometrical analysis of the projection of the interstices in hexagonally close-packed sphere bilayers, slightly etched, on substrates (details in Supporting Information). The dimension of the small and big nanoparticles was represented using their length, *a* and *b*, depicted in Figures 2, 4, and S4 (Supporting Information). On the basis of the top-view and quasi-3D illustration of a plasma-etched bilayer of hexagonally close-packed microspheres (Figures 4 and S4, Supporting Information), *a* can be calculated by the
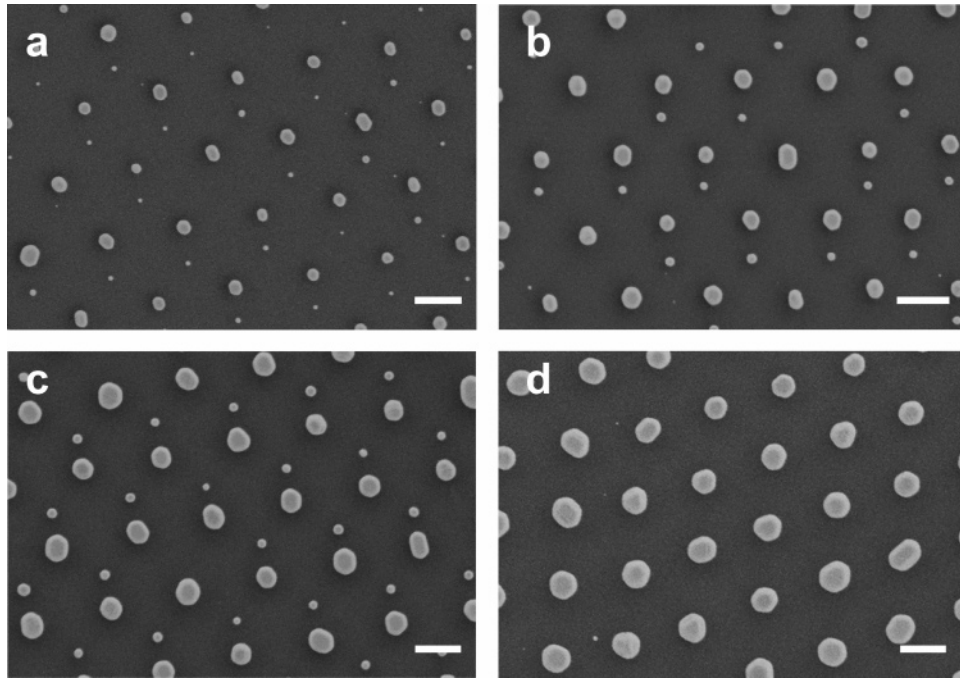
Figure 3. SEM pictures of the hexagonal binary arrays obtained by annealing the Au nanoshuttlecock arrays derived from the hexagonal close-packed 830 nm PS sphere bilayers etched for 10 (a), 20 (b), 25 (c), and 30 min (d). The SEM pictures of the original shuttlecock arrays were shown in Figure 1. The scale bars are 500 nm.

following equations:

$$a = AB = GP = PH - GH \quad (1)$$

$$PH = R \cdot \tan 30° = \frac{R}{\sqrt{3}} \quad (2)$$

$$GH = IJ = (IF - FJ) \quad (3)$$

$$IF = R_1 \cos \theta \quad (4)$$

$$FJ = GJ \cdot \tan \theta \quad (5)$$

$$GJ = HI = O_1H - O_1I \quad (6)$$

$$O_1I = R_1 \cdot \sin \theta \quad (7)$$

$$O_1H = \sqrt{O_1O_5{}^2 - HO_5{}^2} = \sqrt{(R_1 + R_2)^2 - \left(\frac{R}{\cos 30°}\right)^2} = $$
$$\sqrt{(R_1 + R_2)^2 - \frac{4}{3}R^2} \quad (8)$$

$$a = \frac{R}{\sqrt{3}} - R_1 \cdot \cos \theta - R_1 \cdot \tan \theta \cdot \sin \theta + $$
$$\tan \theta \cdot \sqrt{(R_1 + R_2)^2 - \frac{4}{3}R^2} \quad (9)$$

$$a = \frac{R}{\sqrt{3}} + \tan \theta \cdot \sqrt{(R_1 + R_2)^2 - \frac{4}{3}R^2} - \frac{R_1}{\cos \theta} \quad (E1)$$

in which R is the radius of the original spheres, R_1 the radius of the etched upper-layer spheres, and R_2 the radius of the etched lower-layer spheres, respectively. b can be estimated by the following equations:

$$b = BC = PE = PO_6 - EO_6 \quad (10)$$

$$PO_6 = R \cdot \tan 60° = \sqrt{3}R \quad (11)$$

$$EO_6 = \frac{R_2}{\cos \theta} \quad (12)$$

$$b = \sqrt{3}R - \frac{R_2}{\cos \theta} \quad (E2)$$

Table 1 shows that the calculated and experimental values qualitatively agree, but quantitatively they differ by less than 40 nm for b and by a factor of 2 for a. The small deviation for b between experiment and calculation should be due to diffusion and scattering of Au vapor. The large deviation for a should be due to the fact that anisotropic plasma etching rendered the upper-layer spheres oblate-shaped (Figure S5, Supporting Information). After the etched upper-layer spheres were disassembled by ultrasonication, SEM imaging indicated that the maximal polar distances were 60−80% of the equatorial diameters of the etched spheres. As shown in Figures 4b and S4b,c (Supporting Information), one should use the polar distance rather than the equatorial diameter (R_1) of the upper spheres to calculate a. On the basis of the SEM images of the etched colloidal crystals, however, we were able to precise determine only R_1 rather than the polar distances, especially related with calculation of O_1F, O_1H,
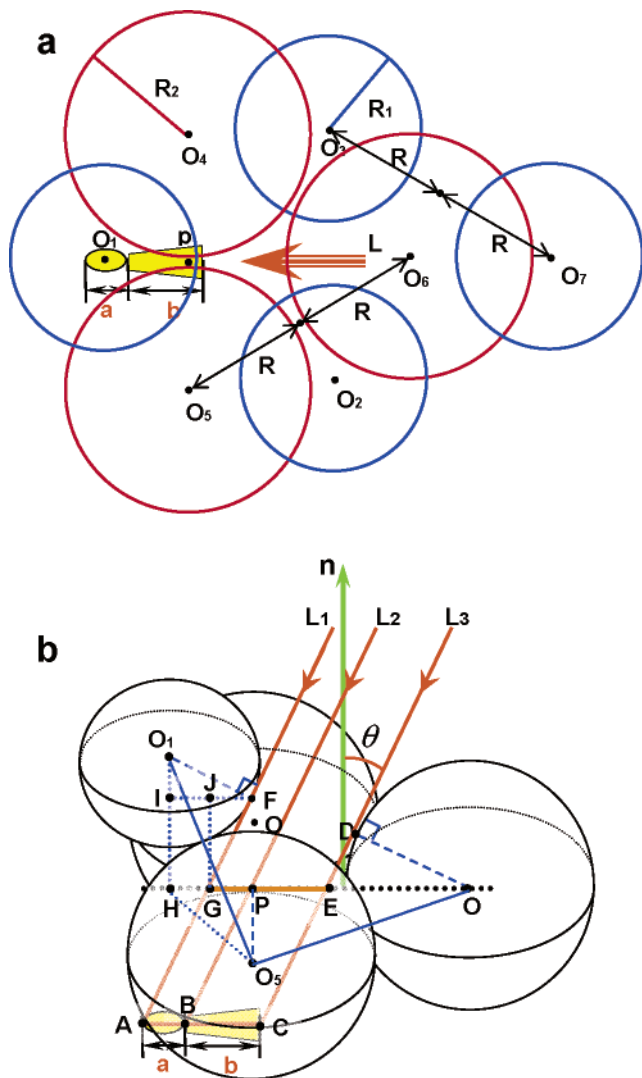
Figure 4. Schematic depictions of the geometric feature of a plasma-etched bilayer of hexagonally close-packed microspheres. (a) Top-view of the etched bilayer, mimicking the structure shown in Figure 2. Three blue circles represent the spheres at the top layer, and three red circles the spheres in the lower layer. R is the radius of the original spheres. O_1, O_2, O_3, and O_7 are the center of the upper layer spheres and O_4, O_5, and O_6, the centers of the lower layer spheres. P is the joint point of the neighboring spheres in the lower layer. The arrow L indicates the incidence direction of Au vapor incidence. (b) Quasi-3D illustration of the etched bilayer. The green line, n, is the normal direction of the equator plane of the three spheres. The orange lines represent the incident Au vapor beam; the incidence angle is θ. L_1 and L_3 are the tangent lines of O_1 and O_6, and the tangent points are F and D, respectively. Assuming no diffraction of the Au vapor beam, the Au vapor flow between L_1 and L_3 can be deposited on the substrate to form small and big nanoparticles, highlighted by yellow. a and b represent the lengths of small and big nanoparticles, and their geometrical evaluation is highlighted by blue lines.

and O_1O_5, and the tangent point of F. In the present modeling, we therefore still assumed that the upper-layer spheres still remained spherical and used R_1 instead of their polar distance, namely, $O_1F = R_1$ and $O_1O_5 = R_1 + R_2$. Provided that the polar distance of the upper-layer spheres were assumed 70% of R_1, the values of a were recalculated

and listed in Table 1, showing a good quantitative agreement with the experimental values.

Concerning the formation of Au nanoshuttlecocks (or binary arrays), we defined three critical incidence angles of Au vapor flow. Obviously, only when the value of a is not zero Au nanosized shuttlecocks appear. The first critical incidence angle (θ_{c1}) was defined at $a = 0$. In the case of 20 min etched bilayers of 830 nm PS spheres, θ_{c1} is 8.8°. In the current work, we found that Au nanosized shuttlecocks were formed only when the incidence angle was larger than 12°, which is rather consistent with our modeling. When a equals b, Au nanoshuttlecocks should not appear, which was used to define the second critical angle (θ_{c2}). θ_{c2} of 20 min etched bilayers of 830 nm PS spheres is calculated as 38.2°. The third critical incidence angle (θ_{c3}) was defined when b equals zero. In this case, the interstitial projection of the masks should be entirely laid on the spheres; no Au is deposited on substrates. θ_{c3} of 20 min etched bilayers of 830 nm PS spheres is 53.6°. When θ is in the range of 38.2−53.6°, a turns out larger than b, accompanied by the appearance of reverse nanoshuttlecocks. Accordingly, we deposited Au on 20 min etched bilayers of 830 nm PS spheres at varied incidence angles.

As shown in Figure 5a, the incidence angle of 30° (close to θ_{c2}) led to Au nanoparticles with a bow-tie shape, which were arranged in a hexagonal array. After 60 min annealing at 900 °C, most of them were retracted into two small round nanoparticles of identical size, which were arranged in deformed hexagonal arrays, but big nanoparticles originating from fusion of two small ones were observed (Figure 5b). When the incidence angle further increased to 45° (between θ_{c2} and θ_{c3}), we were still able to form some Au nanoparticles composed of separated small and big particles in which a was larger than b (Figure 5c). Nonetheless, the integrated nanoparticles from the fusion of small and big particles were also ubiquitously observed. Figure 5d shows that the annealing at 900 °C resulted in structures similar to those obtained using the incidence angle of 30°. The deviation between modeling and experimental data can be due to the nonlinear diffusion and the difficulty of accurate mask registry.

In summary, we successfully demonstrate a facile and versatile methodology, angle-resolved colloidal lithography assisted by plasma etching and postannealing, to fabricate long-range hexagonal binary arrays of Au nanoparticles. The size and shape of both small and big nanoparticles obtained were manipulated by the plasma etching period and the incidence angle of Au vapor flow. The postannealing also provides a powerful way to improve the size and shape monodispersity of the nanoparticles. Similar to the commonly used colloidal lithography, our approach should be independent of constituent spheres and deposition materials, thus providing an immense diversity of the size and chemical composition of nanoparticle binary arrays.

Within the gaps between two metallic particles is an ultrahighly enhanced surface plasmon field, a so-called hot spot, localized, which was between two large particles for
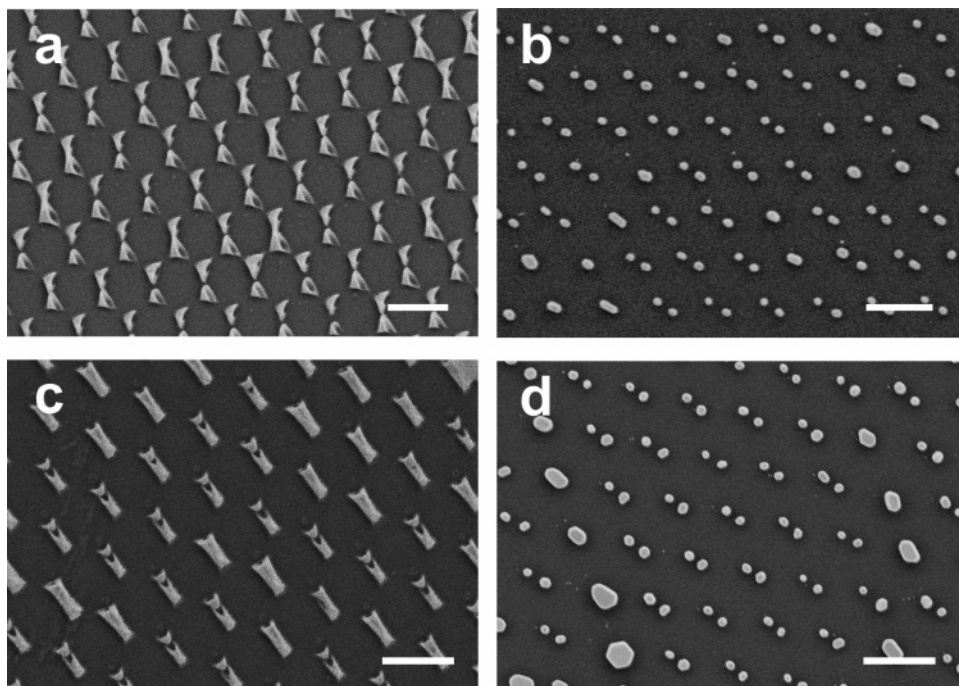
Figure 5. SEM pictures of Au nanoparticle binary arrays obtained by depositing Au on the bilayers of hexagonally close-packed 830 nm PS spheres, etched for 20 min at the incidence angle of 30° (a) and the corresponding arrays after annealing at 900 °C for 60 min at ambient (b). SEM pictures of Au nanoparticle binary arrays derived from the incidence angle of 45° before (c) and after annealing (d). The scale bars are 1 μm.

transverse incident polarization while between small and large particles for longitudinal incident polarization.[11] Owing to the defined but varied separation between the particles, binary hexagonal arrays of Au nanoparticles should provide a good model for study of "hot spot". Our current effort is devoted to formation of Ag nanoparticle binary arrays using different sized PS spheres as templates and theoretical and experimental investigation of surface plasmon field enhancement localized between Ag nanoparticles with identical and different sizes in order to gain an in-depth insight to hot spot.

Supporting Information Available: Details of experimental method. Low-magnification SEM images of a long-range hexagonal array of Au nanoshuttlecocks and its corresponding binary array obtained by annealing at 900 °C. SEM images of a turnup plasma-etched bilayer of hexagonally close-packed 830 nm PS spheres, coated by Au, Au nanoparticle binary arrays obtained by annealing at 700 °C, and the upper-layer spheres disaggregated from 20 min plasma etched bilayers of hexagonally close-packed 830 nm PS spheres. The details of quantitative analysis of the interstitial feature of plasma-etched bilayers of hexagonally close-packed microspheres.

References

(1) For reviews, see: (a) Weller, H. *Angew. Chem., Int. Ed.* **1993**, *32*, 41; (b) Alivisatos, A. *Science* **1996**, *271*, 933; (c) Hu, J.; Odom, T.; Lieber, C. *Acc. Chem. Res.* **1999**, *32*, 435.
(2) For reviews, see: (a) Arden, W. *Curr. Opin. Solid State Mater. Sci.* **2002**, *6*, 371; (b) Gessler, M.; Xia, Y. *Adv. Mater.* **2004**, *16*, 1249; (c) Xia, Y.; Whitesides, G. *Angew. Chem., Int. Ed.* **1998**, *37*, 551.
(3) For reviews, see: (a) Wang, D.; Möhwald, H. *J. Mater. Chem.* **2004**, *14*, 459; (b) Arsenault, A.; Fournier-Bidoz, S.; Hatton, B.; Míguez, H.; Tétreault, N.; Vekris, E.; Wong, S.; Yang, S.; Kitaev, V.; Ozin, G. *J. Mater. Chem.* **2004**, *14*, 781; (c) Xia, Y.; Gates, B.; Yin, Y.; Lu, Y. *Adv. Mater.* **2000**, *12*, 693.
(4) (a) Hulteen, J.; Treichel, D.; Smith, M.; Duval, M.; Jensen, T.; van Duyne R. *J. Phys. Chem. B* **1999**, *103*, 3854. (b) Haynes, C.; van Duyne, R. *J. Phys. Chem. B* **2001**, *105*, 5599. (c) Haynes, L.; McFarland, A.; Smith, M.; Hulteen, J.; van Duyne R. *J. Phys. Chem. B* **2002**, *106*, 1898.
(5) (a) Rybczynski, J.; Ebels, U.; Giersig M. *Colloids Surf. A* **2003**, *219*, 1; (b) Kosiorek, A.; Kandulski, W.; Chudzinski, P.; Kempa, K.; Giersig, M. *Nano Lett.* **2004**, *4*, 1359; (c) Kosiorek, A.; Kandulski, W.; Glaczynska, H.; Giersig, M. *Small* **2005**, *1*, 439; (d) Vossen, D. L. J.; Fific, D.; Penninkhof, J.; van Dillen, T.; Polman, A.; van Blaaderen A. *Nano Lett.* **2005**, *5*, 1175.
(6) (a) Xia, Y.; Kim, E.; Whitesides, G. *Chem. Mater.* **1996**, *8*, 1558; (b) McLellan, J.; Geissler, M.; Xia, Y. *J. Am. Chem. Soc.* **2004**, *126*, 10830.
(7) (a) Burmeister, F.; Schäfle, C.; Keilhofer, B.; Bechinger, C.; Boneberg, J.; Leiderer, P. *Adv. Mater.* **1998**, *6*, 495; (b) Habenicht, A.; Olapinski, M.; Burmeister, F.; Leiderer, P.; Boneberg, J. *Science* **2005**, *309*, 2043.
(8) (a) Choi, D.; Yu, H. K.; Jang, S. G.; Yang, S. M. *J. Am. Chem. Soc.* **2004**, *126*, 7019; (b) von Freymann, G.; John, S.; Kitaev, V.; Ozin, G. A. *Adv. Mater.* **2005**, *17*, 1273.
(9) Zhang, G.; Wang, D.; Möhwald, H. *Chem. Mater.* **2006**, *18*, 3985.
(10) Choi, D.; Kim, S.; Jang, S.; Yang, S.; Jeong, J.; Shin, S. *Chem. Mater.* **2004**, *16*, 4208.
(11) (a) Xu, H.; Kall, M. *Phys. Rev. Lett.* **2002**, *89*, 246802; (b) Kall, M.; Xu, H.; Johansson, P. *J. Raman Spectrosc.* **2005**, *36*, 510.

NL062284C